TRANSIENT ELASTIC STRESS DEVELOPMENT DURING LASER SCRIBING OF CERAMICS

Michael F. Modest
Thomas M. Mallison
Department of Mechanical Engineering
The Pennsylvania State University
University Park, PA 16802

Abstract

Lasers are emerging as a valuable tool for shaping and cutting hard and brittle ceramics. Unfortunately, the large, concentrated heat flux rates that allow the laser to efficiently cut and shape the ceramic also result in large localized thermal stresses in a small heat-affected zone. These notable thermal stresses can lead to micro-cracks, a decrease in strength and fatigue life, and possibly catastrophic failure. In order to assess where, when, and what stresses occur during laser scribing, an elastic stress model has been incorporated into a three-dimensional scribing and cutting code. First, the code predicts the temporal temperature fields and the receding surface of the ceramic. Then, using the scribed geometry and temperature field, the elastic stress fields are calculated as they develop and decay during the laser scribing process. The analysis allows the prediction of stresses during continuous wave and pulsed laser operation, a variety of cutting speeds and directions, and various shapes and types of ceramic material. The results of the analysis show substantial tensile stresses develop over a thick layer below and parallel to the surface, which may be the cause of experimentally observed subsurface cracks.

Nomenclature

a	stress constant
c_p	specific heat of ceramic, [J/(kg K)]
E	modulus of elasticity, [Pa]
E_h	decomposition energy, [J/kmol]
Δh_{re}	ablation enthalpy, [J/kg]
$\mathbf{F}$	laser irradiation flux vector, [W/m^2)]
F_0	laser irradiation flux at center of beam, [W/m^2)]
k	thermal conductivity, [W/(m K)]
L, W, H	length, width, thickness of ceramic workpiece, [m]
$\hat{\mathbf{n}}$	unit surface normal pointing into workpiece,
N_k	Conduction-to-laser power parameter
$s, \bar{s}$	(non-dimensional) hole depth, [m]
Ste	Stefan number
$t, \bar{t}$	(non-dimensional) time, [s]
T	temperature, [K]
$\underline{\underline{u}}, \bar{\underline{\underline{u}}}$	(non-dimensional) displacement vector, [m]
u, v, w	displacements in x, y, and z directions, respectively,
v_n	total surface recession speed [m/s]
w_0	focal radius of laser beam [m]
$x, y, z,$	non-dimen. Cartesian coordinates, [m]
α	coefficient of thermal expansion, [K^{-1}]
α_{abs}	laser absorptance,
$\underline{\underline{\delta}}$	identity tensor,
$\underline{\underline{\epsilon}}, \bar{\underline{\underline{\epsilon}}}$	(non-dimensional) strain tensor, [-]
ϵ	Average of trace for the strain tensor
κ	absorption coefficient of ceramic, [cm^{-1}]
μ	Lamé elastic constant , [Pa]
ν	Poisson's ratio, [-]
ρ	density of ceramic, [kg/m^3]
$\underline{\underline{\sigma}}, \bar{\underline{\underline{\sigma}}}$	(non-dimensional) stress tensor, [Pa]
ξ, η, ζ	computational coordinates,
θ	non-dimensional temperature
Subscripts	
∞	at ambient, or at far-away conditions
re	at removal temperature
x, y, z	x, y, z-components
Superscripts	
$-$	dimensional quantity

Introduction

Various types of ceramics appear to be excellent candidates for high-temperature, high-load applications due to their high-temperature strength, oxidation resistance, and thermal shock resistance. However, because ceramics are so brittle, they are susceptible to cracking during machining and are extremely hard to fabricate and machine into delicate or complex parts. Most ceramics can be efficiently scribed or cut with a laser, although many aspects of this process are still poorly understood. During laser machining of ceramics, laser irradiation produces thermal stresses that often result

in micro-cracks and even catastrophic failure; in all cases laser processing severely reduces the bending strength of the ceramic (Copley et al. [1], Yamamoto and Yamamoto [2], deBastiani, Modest and Stubican [3](.

Most analytical investigations have been limited to thermoelastic bodies using one-dimensional analysis or commercial finite element programs. Hasselman *et al.* [4–6] subjected a one-dimensional slab to external radiation to investigate the transient thermal stress field. He found the largest tensile stresses occurred in slabs of medium optical thickness ($\kappa H \sim 3$ to 5) with κ being the absorption coefficient of the ceramic. Bradley [7] performed a similar analysis for an opaque slab using a procedure to describe the total strain energy at fracture due to the thermal stresses. Sumi *et al.* [8] used an analytical/numerical solution for transient stresses for a simplified 3-D problem. He described a local square surface heat source moving in the x-direction across an infinite flat plate in the x-y-plane. The results were a largely compressive stress field with some small tensile stresses. However, the tensile stresses did appear near the edge of the heat source. Ferrari and Harding [9] used a one-dimensional, ceramic-coated sphere to simulate the residual thermal stress field. They observed moderate compressive stresses in the radial direction, and large tensile stresses in the transverse direction. Gross *et al.* [10] investigated crack formation in thin silicon wafers during drilling with CO_2 and Nd-YAG lasers. They developed a simple one-dimensional model incorporating compressive plastic deformation to predict the thermal stresses. The model predicted that during cooldown, the residual circumferential stresses are in tension in the deformation zone and are in compression outside the deformation zone. The model also predicted the radial thermal stresses are tensile everywhere with a maximum at the deformed zone boundary. Experimentally, they observed radial cracks that extended to the deformed zone boundary and circumferential cracks that followed the zone boundary. Both types of cracks confirmed qualitatively the nature of the theoretically predicted stress. Modest [11] also developed a two-dimensional, axisymmetric model for laser drilling of ceramics. The model was able to handle CW and pulsed laser operation and elastic as well as viscoelastic stress calculations. He noted that during drilling, substantial hoop and normal tensile stresses develop over a thick layer below and parallel to the surface. These stresses could result in experimentally observed subsurface cracks in the same region. He also found that viscoelastic effects were mostly limited to an extremely thin layer near the ablation front. There the ceramic had softened, relaxing the compressive stresses during heating and causing strong tensile stresses during cooling.

In the present paper our three-dimensional laser machining code has been augmented by an elastic stress model, to predict thermal stresses as they develop during CW and pulsed laser scribing of ceramics.

Theoretical Background

Modest [12] used several assumptions in order to obtain a realistic, yet mathematically simple description of the laser scribing process. Although the heat transfer code allows for many scenarios, the following assumptions will be used in the present stress model:

1. The solid is isotropic, has constant density, and is opaque, *i.e.*, the laser beam does not penetrate appreciably into the solid.
2. The solid moves with constant velocity.
3. Change of phase from solid to vapor occurs in a single step with a rate governed by a single Arrhenius relation.
4. The evaporated material does not interfere with the incoming laser beam (or is removed by an external gas jet).
5. The heat transfer properties are temperature independent.
6. Heat losses by convection and re-radiation are small compared to conduction.
7. Multiple reflections of laser radiation within the groove are neglected, restricting the model to shallow holes, holes with steep sidewalls, or material with high absorptivity.
8. Heat transfer is unaffected by thermal expansion (always true for opaque ceramics as shown by an order of magnitude analysis).

In addition the following assumptions are made for the stress calculations:

1. The mechanical properties, such as the modulus of elasticity, are temperature independent.
2. Displacements are small quantities that vary over the entire volume. Large displacements, such as buckling of thin plates are not allowed.
3. No external forces are applied to the solid. Stresses occur only due to thermal expansion or contraction.
4. Inertia effects are negligible during stress development (always true of opaque ceramics, but may break down for semitransparent ceramics subjected to ns laser pulsing).

Heat Transfer The heat transfer model developed by Roy and Modest [13] is summarized here. The transient conduction equation for a solid workpiece of dimensions $L \times W \times H$, irradiated by a Gaussian laser beam may be expressed in terms of temperature as (see Fig. 1):

$$\rho c_p \frac{\partial T}{\partial t} = \nabla \cdot (k \nabla T) \tag{1}$$

subject to the boundary conditions

$$\bar{x} = 0 \ : \ T \rightarrow T_\infty \qquad \bar{x} = L \ : \ T \rightarrow T_\infty \tag{2a}$$

$$\bar{y} = 0 \ : \ T \rightarrow T_\infty \qquad \bar{y} = W \ : \ T \rightarrow T_\infty \tag{2b}$$

$$\bar{z} = 0 \ : \ \alpha_{\text{abs}} \, \mathbf{F} \cdot \hat{\mathbf{n}} = - \hat{\mathbf{n}} \cdot (k \nabla T) + v_n \rho \Delta h_{\text{re}} \tag{2c}$$

$$\bar{z} = H \ : \ \frac{\partial T}{\partial \bar{z}} = 0 \tag{2d}$$

and appropriate initial conditions such as

$$\bar{t} = 0 \ : \quad T(\bar{x}, \bar{y}, \bar{z}, 0) = T_\infty \tag{3}$$

$$s(\bar{x}, \bar{y}, \bar{z}, 0) = \bar{s}_0(\bar{x}, \bar{y}, \bar{z}) \tag{4}$$

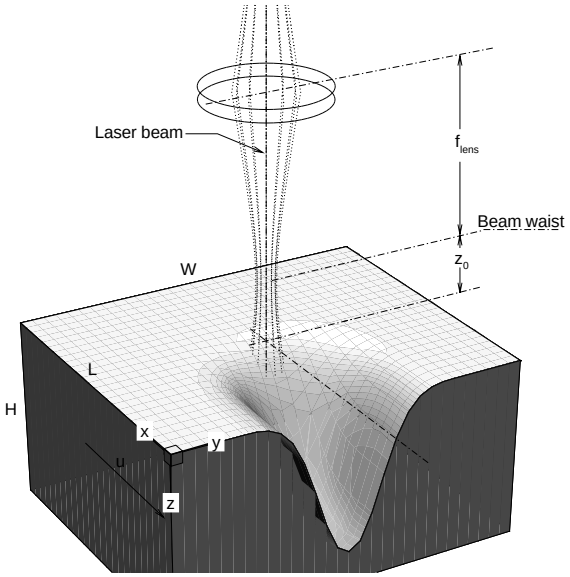

Figure 1: Laser scribing setup and coordinate system

where ρ, c_p, k, and α_{abs} are the density, specific heat, thermal conductivity, and the material's absorptance, respectively; $\bar{x}$, $\bar{y}$, and $\bar{z}$ are the Cartesian coordinates and $\bar{s}$ is the local depth of the groove under the laser (*i.e.*, the $\bar{z}$-coordinate of the top surface); $\hat{\mathbf{n}}$ is the unit vector normal to the surface pointing into the solid; v_n is the total surface recession velocity during scribing, and $\mathbf{F}$ is the irradiation intensity distribution. The overbar quantities distinguish the present dimensional quantities from the non-dimensional quantities below. The boundary conditions are sufficient to solve equation (1) for the temperature distribution, if the shape of the hole is known. The previous work assumes that ablation/decomposition of the solid material is governed by a simple equation of the Arrhenius type. This relation gives the rate of mass loss per unit area as

$$\dot{m}'' = \rho v_n = \rho C_1 e^{-E_h / \bar{R} T} \tag{5}$$

where E_h is the decomposition energy, $\bar{R}$ is the universal gas constant, and C_1 is a preexponential factor that depends on the type of ablation.

The governing equations and boundary conditions are non-dimensionalized using the beam radius at the focal point, w_0, and the ablation temperature of the material, T_{re}:

$$x = \frac{\bar{x}}{w_0} \qquad y = \frac{\bar{y}}{w_0} \qquad z = \frac{\bar{z}}{w_0} \qquad t = \frac{k \bar{t}}{\rho c_p w_0^2} \qquad s = \frac{\bar{s}}{w_0} \qquad \theta = \frac{T - T_\infty}{T_{\text{re}} - T_\infty} \tag{6}$$

This leads to two basic non-dimensional parameters governing the laser/material interaction:

$$N_k = \frac{k (T_{\text{re}} - T_\infty)}{F_0 w_0} \qquad \text{Ste} = \frac{\Delta h_{\text{re}}}{c_p (T_{\text{re}} - T_\infty)} \tag{7}$$

Boundary-fitted coordinates are employed for the numerical solution. A detailed discussion can be found in Roy and Modest [13].

Thermal Stresses The extreme temperature gradients that occur during laser machining result in large, localized thermal expansion. This thermal expansion, in turn, causes large thermal stresses in the ceramic. While under most conditions ceramics may be considered elastic, during laser machining there will be a thin zone near the receding surface where significant creep may occur. Theoretically, stress distributions for the shapes and temperature distributions obtained from the heat transfer code can be determined using a commercial finite-element package. However, the extreme temperature gradients normal to the top surface encountered during laser machining necessitate extreme aspect ratios for the finite volumes (up to 1000:1 and more), which precludes the use of such commercial finite-element codes. In the present first attempt to quantify the thermal stresses during laser scribing, the influence of the thin creep zone near the top surface will be neglected, since it's contribution to the overall stress field is expected to be small [11].

Under the conditions given by the heat transfer portion, the stress distribution is solved using the following sets of equations. The first set is the non-dimensional governing equation for the entire stress distribution of the part, $\nabla \cdot \underline{\underline{\sigma}} = 0$, or after expansion into three equations,

$$\frac{\partial \sigma_{xx}}{\partial x} + \frac{\partial \tau_{xy}}{\partial y} + \frac{\partial \tau_{xz}}{\partial z} = 0, \quad \frac{\partial \tau_{xy}}{\partial x} + \frac{\partial \sigma_{yy}}{\partial y} + \frac{\partial \tau_{yz}}{\partial z} = 0, \quad \frac{\partial \tau_{xz}}{\partial x} + \frac{\partial \tau_{yz}}{\partial y} + \frac{\partial \sigma_{zz}}{\partial z} = 0 \tag{8}$$

The second set are the constitutive equations, in nondimensional form, relating the stress and the strain, and the strain and the displacement for an elastic body, as given by Boley and Weiner [14]:

$$\sigma_{ij} = \epsilon_{ij} + \delta_{ij}\left[a\epsilon - (a+1)\theta\right] \;\; ; \quad \epsilon_{ij} = \frac{1}{2}\left(\frac{\partial u_i}{\partial x_j} + \frac{\partial u_j}{\partial x_i}\right) \tag{9}$$

where $\sigma_{11} = \sigma_{xx}$, $\sigma_{12} = \tau_{xy}$, $\epsilon_{11} = \epsilon_{xx}$, $\epsilon_{12} = \epsilon_{xy}$, etc., $\epsilon = \frac{1}{3}\left(\epsilon_{xx} + \epsilon_{yy} + \epsilon_{zz}\right)$ and the following non-dimensional quantities are defined as:

$$\underline{\underline{\sigma}} = \frac{\bar{\bar{\sigma}}}{2\mu\alpha\left(T_{\text{re}} - T_\infty\right)}; \quad \underline{\epsilon} = \frac{\bar{\bar{\epsilon}}}{\alpha\left(T_{\text{re}} - T_\infty\right)}; \quad \underline{u} = \frac{\bar{\bar{u}}}{w_0\alpha\left(T_{\text{re}} - T_\infty\right)}; \quad a = \frac{3\nu}{(1-2\nu)} \tag{10}$$

where μ is Lamé's elastic constant (= G, the shear modulus), ν is Poisson's ratio, and α is the coefficient of linear expansion.

Expanding and inserting the relationships from equation (9) produces the equations for the stress components in terms of the displacements:

$$\sigma_{xx} = \frac{a}{3}\left(\frac{\partial u}{\partial x} + \frac{\partial v}{\partial y} + \frac{\partial w}{\partial z}\right) + \frac{\partial u}{\partial x} - (a+1)\theta \tag{11}$$

$$\sigma_{yy} = \frac{a}{3}\left(\frac{\partial u}{\partial x} + \frac{\partial v}{\partial y} + \frac{\partial w}{\partial z}\right) + \frac{\partial v}{\partial y} - (a+1)\theta \tag{12}$$

$$\sigma_{zz} = \frac{a}{3}\left(\frac{\partial u}{\partial x} + \frac{\partial v}{\partial y} + \frac{\partial w}{\partial z}\right) + \frac{\partial w}{\partial z} - (a+1)\theta \tag{13}$$

$$\tau_{xy} = \tau_{yx} = \frac{1}{2}\left(\frac{\partial u}{\partial y} + \frac{\partial v}{\partial x}\right), \quad \tau_{xz} = \tau_{zx} = \frac{1}{2}\left(\frac{\partial u}{\partial z} + \frac{\partial w}{\partial x}\right), \quad \tau_{yz} = \tau_{zy} = \frac{1}{2}\left(\frac{\partial v}{\partial z} + \frac{\partial w}{\partial y}\right) \tag{14}$$

The governing equation, equation (8), is an elliptic vector equation requiring three boundary conditions at each surface point. The surface perpendicular to the laser beam ($z = s$ and $z = H$) have a no-traction boundary condition, $\underline{\underline{\sigma}} \cdot \hat{\mathbf{n}} = 0$, and the side surfaces parallel to the laser beam ($x = 0,\ y = 0,\ x = L$, and $y = W$) have either no-traction or clamped boundary conditions. If the heat affected zone of an actual workpiece is confined to a small internal area, it is reasonable to confine the calculations to a smaller piece containing the heat affected zone, together with a clamped boundary condition. On the other hand for operations where the laser is near the edge of the part or where significant temperature gradients remain at the edge of the part, the no-traction boundary condition must be invoked on that boundary. For the present research all operations are assumed to take place on a small heat affected zone in the middle of a large part.

Inserting equations (11) through (14) into equations (8) and applying the boundary conditions gives a set of equations in terms of displacements, from which the stress distribution of the entire part can be determined. This final set of three equations in three unknowns contains partial derivatives of the displacement vector that must be solved numerically. The numerical solution follows the approach of the ablation code as given by Roy and Modest [13]. From this previous work the temperature field, and equally important, the shape of the part, are known. The stress code will use the temperature field and the shape of the part as inputs. After a coordinate transformation from physical to computational coordinates, as outlined by Thompson, Warsi, and Mastin [15], and finite differencing, the code solves the displacement field using an over-relaxation scheme with a block-tridiagonal solver. Special consideration must be given at the no-traction boundaries because of the out-of-plane derivatives. The internal node equations and the no-traction boundary condition equations are combined to remove the desired out-of-plane derivatives using integration over half-nodes adjacent to the surface. After long and tedious manipulations (not shown), the result is a set of three equations for each of the $N_\xi \times N_\eta \times N_\zeta$ nodes that forms the overall grid (cutting through is not allowed for the present stress calculations). The final nineteen point stencil is of the form:

$$\underline{\underline{p}}_{ijk}\underline{\phi}_{i,j,k} = \underline{\underline{n}}_{ijk}\underline{\phi}_{i,j+1,k} + \underline{\underline{s}}_{ijk}\underline{\phi}_{i,j-1,k} + \underline{\underline{e}}_{ijk}\underline{\phi}_{i+1,j,k} + \underline{\underline{w}}_{ijk}\underline{\phi}_{i-1,j,k} + \underline{\underline{t}}_{ijk}\underline{\phi}_{i,j,k+1} + \underline{\underline{b}}_{ijk}\underline{\phi}_{i,j,k-1}$$

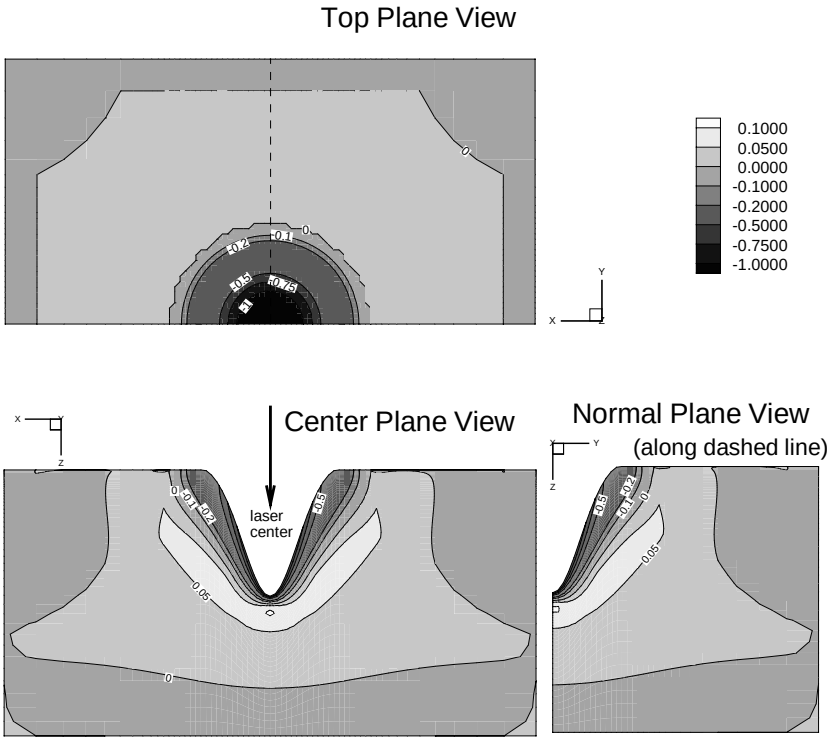

Figure 2: Principal stress distribution during CW CO_2 laser drilling; time = 1.8 ms

$$+\underline{\underline{ne}}_{ijk}\left(\underline{\phi}_{i+1,j+1,k}+\underline{\phi}_{i-1,j-1,k}-\underline{\phi}_{i+1,j-1,k}-\underline{\phi}_{i-1,j+1,k}\right)+\underline{\underline{te}}_{ijk}\left(\underline{\phi}_{i+1,j,k+1}+\underline{\phi}_{i-1,j,k-1}-\underline{\phi}_{i+1,j,k-1}-\underline{\phi}_{i-1,j,k+1}\right)$$
$$+\underline{\underline{tn}}_{ijk}\left(\underline{\phi}_{i,j+1,k+1}+\underline{\phi}_{i,j-1,k-1}-\underline{\phi}_{i,j+1,k-1}-\underline{\phi}_{i,j-1,k+1}\right)+\underline{R}_{ijk} \quad (15)$$

Equation (15) is a system of linear equations in the form $\underline{\underline{A}}\,\underline{\phi}=\underline{R}$, where $\underline{\underline{A}}$ is a coefficient matrix, whose overall dimension is determined by the number of nodes and where each individual component is a 3×3 matrix (for example $\underline{\underline{p}}_{ijk}$). The solution vector, $\underline{\phi}$, is the displacement vector, and the right-hand-side vector, $\underline{R}$, contains the temperature gradients at the interior nodes and temperatures at the boundary nodes. Once the displacement field is known the strain and stress fields are easily obtained using equation (9) and equations (11) to (14). Finally, the principal stresses are the eigenvalues for the stress matrix, sorted by magnitude, at each node.

Results and Discussion

The stress code can calculate many possible scenarios. Coupled with the flexibility of the heat transfer code, the number of outputs is endless. The code is designed to assist engineers in improving the laser machining process. For brevity, only a few scenarios are presented here that include scribing operations for a CW laser and a conventionally-pulsed laser, with pulse duration on the order of hundreds of microseconds. The simulated material is silicon carbide because of its wide range of applications. The pertinent material properties for silicon carbide at 1500 °C are given in Table 1. All these material properties are assumed to be temperature independent.

Table 1: Properties of Silicon Carbide

Thermal		Mechanical	
T_{re}	3000 K	ρ	3185 kg/m^3
c_p	1359 J/(kg K)	ν	0.17
k_h	17.3 W/(m K)	α	4.02 $\times 10^{-6}$/K
Δh_{re}	12.1 MJ/kg	μ	175 GPa
α_{abs}	0.9		
Ste	3.3		

The laser simulated is a typical CO_2 laser (such as the one in our laboratory), with a beam radius of w_0=170 μm and absorbed laser power of αP=600 W. The speed of the laser for all of the scribing operations is 10 cm/sec. The simulated silicon carbide workpiece has the non-dimensional dimensions of $12\times 12\times 5$ (or 2 mm $\times$ 2 mm $\times$ 0.85 mm). As previously mentioned, actual workpieces tend to have much larger length and width dimensions, although stresses decay rapidly beyond the heat affected zone. Thus, smaller dimensioned workpieces, clamped on all sides, have

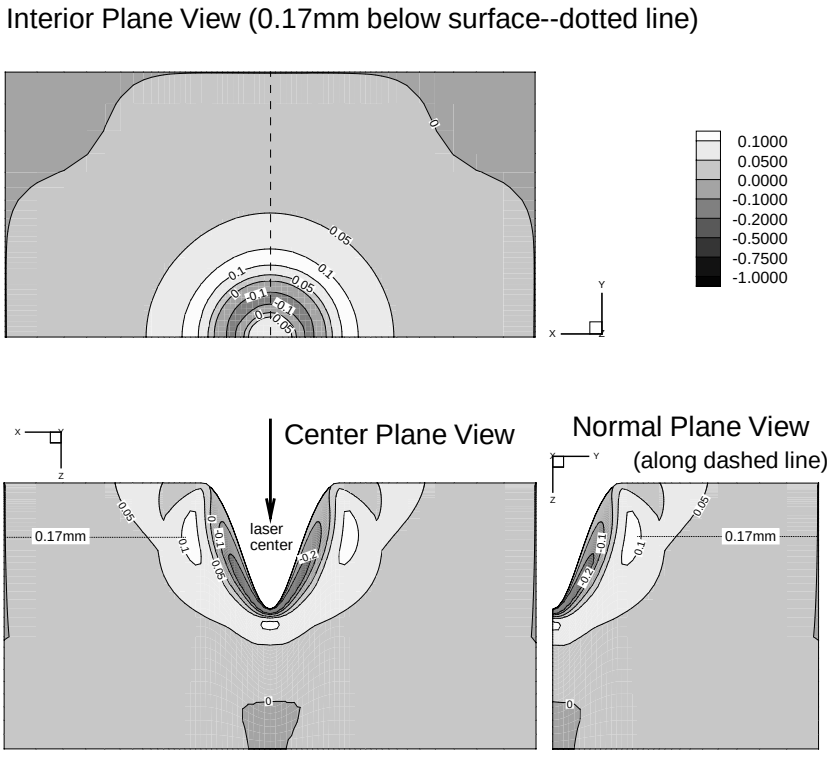

Figure 3: Maximum principal stress distribution during CW CO_2 laser drilling; time = 1.8 ms

essentially the same stress distributions, but the stress distributions can be calculated on a smaller piece much more rapidly.

The first simulation is a drilling operation with a CW laser to allow comparison with our previous two-dimensional model (Modest [11]), and to highlight the differences between drilling and scribing. This is followed by a CW scribing operation starting the laser in the pre-drilled hole to investigate the development of the stress distributions. Finally, CW and pulsed laser operations are compared for a pure scribing operation.

The principal stresses are sorted by magnitude and the results shown are the maximum principal stress, which generally consist of stresses in the direction normal to the top surface, and the intermediate principal stress that generally consists of stresses in the radial and hoop directions. The smallest principal stress is always compressive and, thus, uninteresting and is not shown.

Figures 2 and 3 show the half-views of the principal stresses for laser drilling lasting 1.8ms. The stresses are symmetric about the x and y-axes, with the laser positioned over the center of the workpiece. Figure 2 shows the intermediate principal stress distribution, composed primarily of hoop stresses in the heat affected zone and radial stresses elsewhere, with a large tension sheet above 0.05 (190 MPa) in a region just outside the heat affected zone. There are large compressive stresses directly under the laser, limited to a thin layer near the surface, and a small spot with strong tension (above 0.1 or 400MPa inside the material directly under the laser center). Figure 3 shows the maximum principal stresses whose directions are primarily normal to the top surface. The only exception is the lobe of maximum principal stress extending from the interior tensile region to the top surface, as shown in the normal and center plane views of Fig. 3. In this tensile region the maximum principal stress is in the radial direction. The maximum tension is 0.11 (440 MPa) in a ring approximately 0.17 mm below the top surface, just outside the heat affected zone.

Figure 4 gives the maximum principal stress distributions for laser scribing starting in a previously drilled hole and shows the stress field skewing and shifting to the region in front of the laser. Lasing conditions are identical to the drilling case, except that the laser starts moving after t=1.8 ms (i.e., the time in Figs. 2 and 3), with a velocity of 10 cm/sec in the positive x-direction. The intermediate principal stresses are very similar to those for pure drilling (Fig. 2), and are not shown here. The maximum principal tensile stress (shown in Fig. 4) moves toward the region in front of the laser and increases to .115 (440 MPa), with its direction being normal to the top surface. This tension region is now in the shape of a moon crescent, with less tension behind the laser. The shift in the stress fields is due to the fact that the hot region behind the moving laser is spreading and becoming larger than in front of the laser. This again causes sharper temperature gradients (and, thus, larger stresses) ahead of the laser than in the cool-down zone behind it.

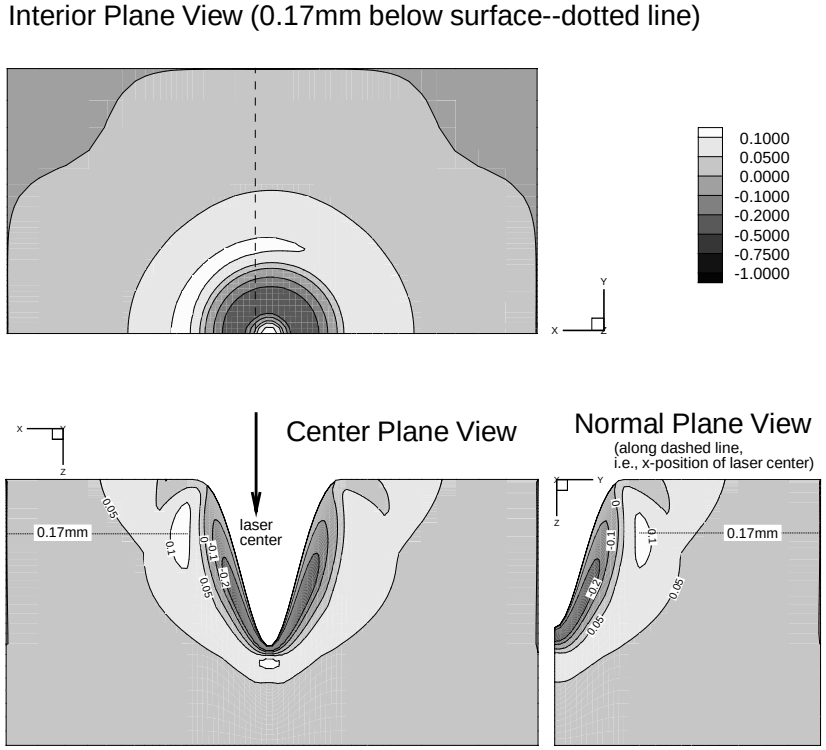

Figure 4: Maximum principal stress distribution during CW CO_2 laser scribing commencing after drilling for 1.8 ms; time = 2.5 ms

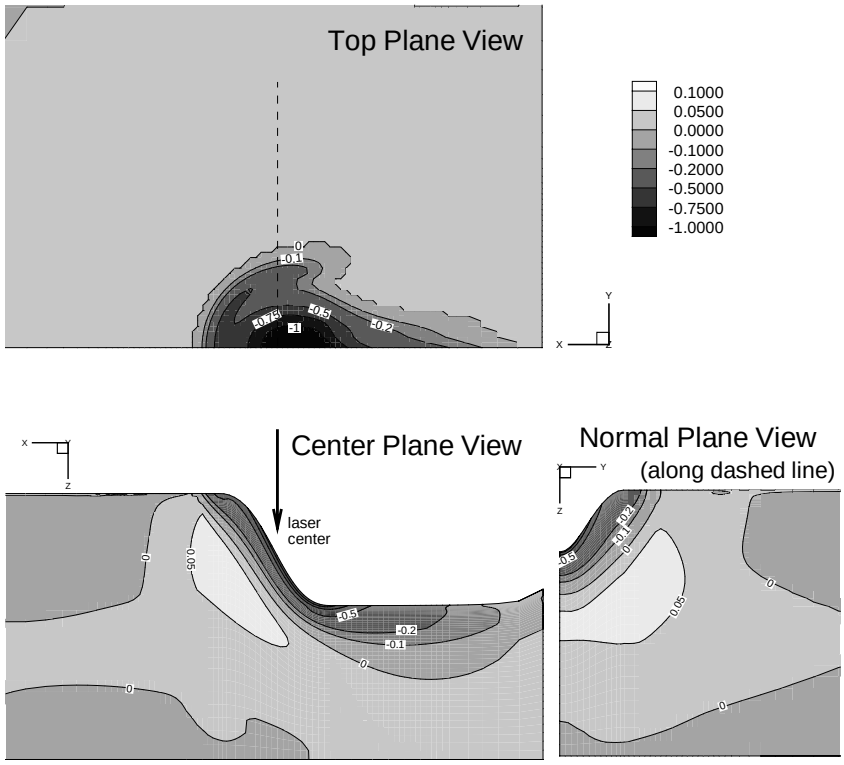

Figure 5: Principal stress distribution during CW CO_2 laser scribing; time = 2.5 ms

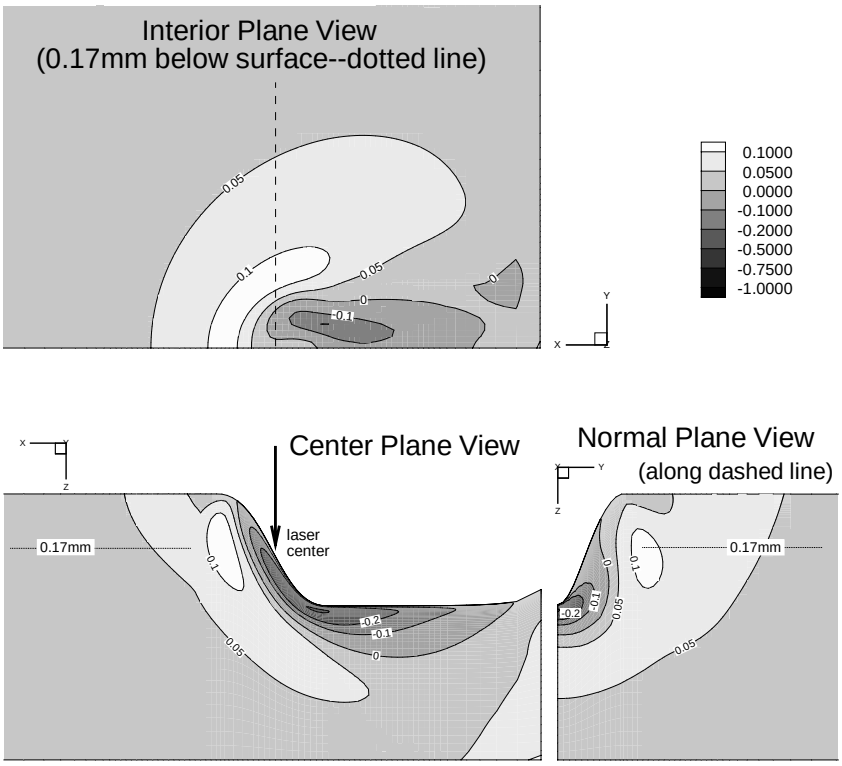

Figure 6: Maximum principal stress distribution during CW CO_2 laser scribing; time = 3.5 ms

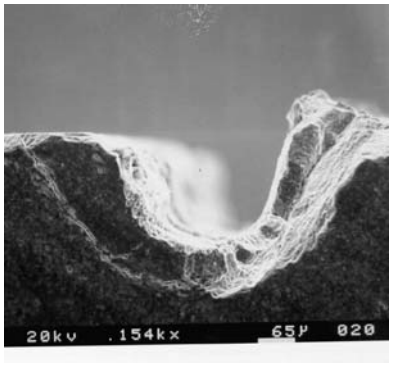

Figure 7: SEM cross-section of CW CO_2 laser scribed of α-SiC (power P = 600 W, laser scan velocity = 5 cm/s)

For the pure scribing case (with the laser scanning onto the workpiece from otside) three of the side surfaces have been assumed clamped, while the no-traction boundary condition was applied at $x = 0$ where the laser scans onto the surface. For pure scribing the shifting and twisting of the stress fields is more dramatic. As shown in Fig. 5 for CW laser scribing, the subsurface tensile region has completely shifted to the front and the sides of the laser. Additionally, there is a region of tension forming close to the top surface near the edge of the groove behind the laser. This is due to the region behind the laser expanding outward faster, causing the material to tear near the edge of the groove. Again, the intermediate principal stresses are primarily hoop stresses in the heat affected zone and radial stresses outside the heat affected zone. The dramatic shift in the stress fields is also visible in Fig. 6, which shows the maximum principal stresses are primarily in the direction normal to the top surface, with a lobe of radial stresses extending from the interior tension region to the top surface in front of the laser. For the pure scribing case there is no subsurface tensile region behind the laser as there was in the drilling and pre-drilling cases. Figure 6 also shows increased tension in the maximum principal stresses in front of the laser, at 0.17 mm below the top surface, with a maximum value of 0.126 (480 MPa). On a qualitative level the results explain beautifully the damage we have routinely observed when scribing α-SiC with our CW CO_2 laser (see, *e.g.*, Fig. 7, which shows α-SiC scribed at 5 cm/sec and CW power of 600 W; this particular photo was chosen because it displays much-stronger-than-average thermal stress damage).

There is a substantial difference in the temperature profiles between a pulsed laser and a continuous wave laser. The heat affected zone for the pulsed laser scribing case is consistently shallower than for the CW case. Even for a laser with a relatively long pulse duration ($\sim$1 ms), the groove becomes much deeper since there are much lower conduction losses into the material. In general, temperature gradients during pulsed laser operation are much larger, and because they occur over such a short depth, the stress fields are more concentrated. In our sample calculations, average absorbed laser power is again 600 W with a duty cycle of 25% (on-time is 25% of total pulse time). The total duration of the operation is such that the total amount of energy released into the part is the same as for the CW laser scribing case, as shown in Figs. 5 and 6. Figure 8 shows the combination of hoop and radial principal stresses for the pulsed laser scribing case as they exist at the end of a pulse (i.e., just before the laser shuts off). It is seen that the stress field,

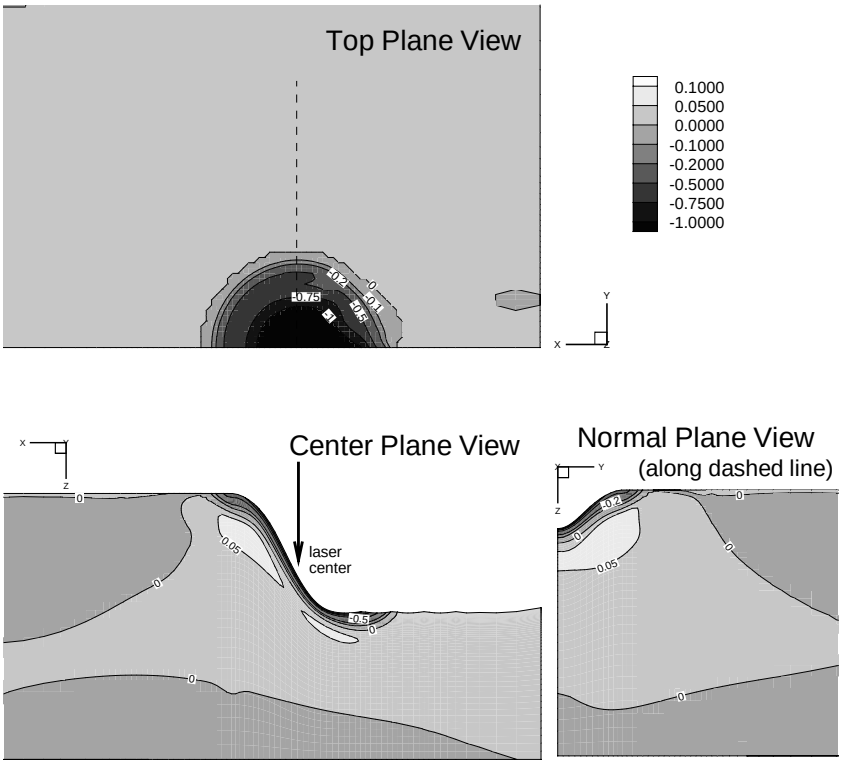

Figure 8: Principal stress distribution during pulsed CO_2 laser scribing; time = 2.2 ms

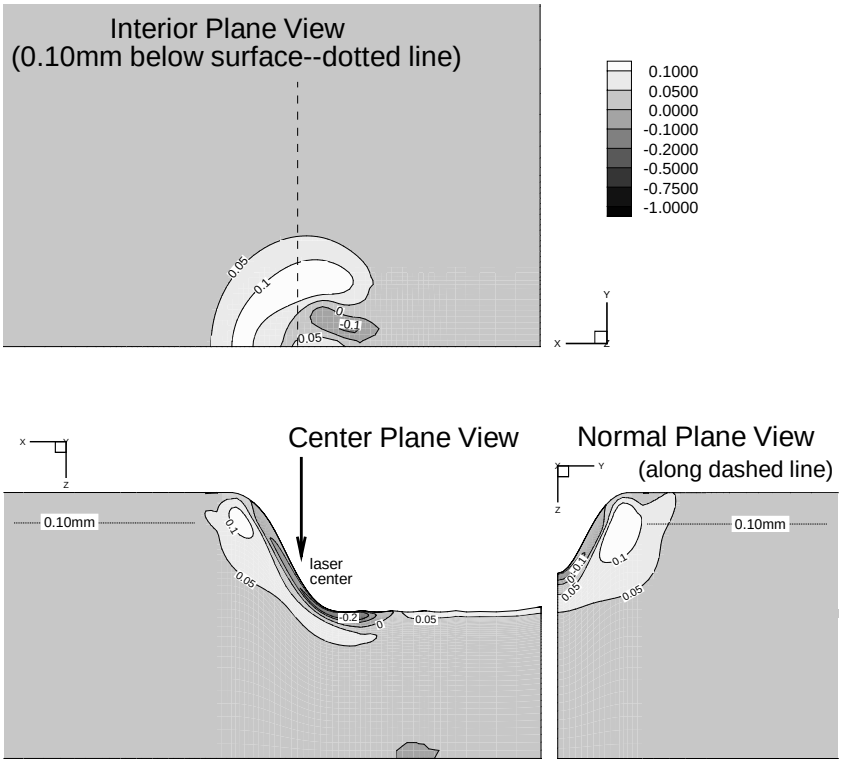

Figure 9: Maximum principal stress distribution during pulsed CO_2 laser scribing; time = 2.2 ms

compression as well as tension, are thinner in depth, and smaller in area, with a much shorter cool-down tail, essentially following the trends of the much thinner and smaller (in area) heat-affected zone during pulsed scribing. Surprisingly, pulsing has little effect on the magnitude of hoop and radial stresses. The maximum normal principal stress, shown in Fig. 9, is higher for the pulsed laser scribing operation, the maximum value being 0.178 (675 MPa) located to the side of the laser, while in the CW case the maximum tension was in front of the laser.

Conclusions

To investigate the stress distributions during CW and pulsed laser scribing of ceramics, an elastic stress model has been incorporated into our three-dimensional machining code. Simulations have been performed on thin wafers of silicon carbide to observe the development of the stress distributions. The stress fields for the scribing operations are non-symmetric and shift to the region in front of the laser as compared to the drilling operation. For the simulated CW conditions, the maximum principal stress was found to be 480 MPa in a direction normal to the surface and located in front of the laser just outside the heat affected zone. The maximum principal stress shows, on a qualitative level, the damage observed during experimental laser scribing. The intermediate principal stress consists of compressive hoop stresses in the heat affected zone and smaller tensile radial stresses outside the heat affected zone. For CW and pulsed scribing a region of tensile stresses forms below the surface near the edge of the groove to the side and behind of the laser. For pulsed laser scribing, stress fields are considerably more compact but, with the exception of normal tensile stresses, not greatly increased. The maximum principal stress for pulsed laser scribing is again normal to the surface, but located to the side of the laser with a value of 675 MPa for the conditions simulated here.

Acknowledgments

Support by the National Science Foundation through Grant no. CMS-9634744 is gratefully acknowledged.

References

1. Copley, S. W., R. J. Wallace, and M. Bass (1983), Laser Shaping of Materials, In *Lasers in Materials Processing* (Edited by Metzbower, E. A.), American Society for Metals, Metals Park, Ohio.
2. Yamamoto, J., and Y. Yamamoto (1987), Laser Machining of Silicon Nitride, In *International Conference on Laser Advanced Materials Processing – Science and Applications*, 297–302. High Temperature Society of Japan, Japan Laser Processing Society, Osaka, Japan.
3. DeBastiani, D., M. F. Modest, and V. S. Stubican (1990), Mechanisms of Reactions During CO_2-Laser Processing of Silicon Carbide, **J. Amer. Cer. Soc. 73**(7), 1947–1952.
4. Hasselman, D. P. H., J. R. Thomas, M. P. Kamat, and K. Satyamurthy (1980), Thermal Stress Analysis of Partially Absorbing Brittle Ceramics Subjected to Symmetric Radiation Heating, **J. Amer. Cer. Soc. 63**(1-2), 21–25.
5. Thomas, J. R., J. P. Singh, and D. P. H. Hasselman (1981), Analysis of Thermal Stress Resistance of Partially Absorbing Ceramic Plate Subjected to Asymmetric Radiation, I: Convective Cooling at Rear Surface, **J. Amer. Cer. Soc. 64**(3), 163–173.
6. Singh, J. P., N. Sumi, J. R. Thomas, and D. P. H. Hasselman (1981), Analysis of Thermal Stress Resistance of Partially Absorbing Ceramic Plate Subjected to Asymmetric Radiation, II: Convective Cooling at Front Surface, **J. Amer. Cer. Soc. 64**, 169–173.
7. Bradley, F. (May 1988), Thermoelastic Analysis of Radiation-Heating Thermal Shock, **High Temperature Technology 6**(2), 63–72.
8. Sumi, N., R. B. Hetnarski, and N. Noda (1987), Transient Thermal Stresses due to a Local Source of Heat Moving over the Surface of an Infinite Elastic Slab, **Journal of Thermal Stresses 10**, 83–96.
9. Ferrari, M., and J. H. Harding (1992), Thermal Stress Field in Plasma-Sprayed Ceramic Coatings, **Journal of Energy Resources Technology 114**, 105–109.
10. Gross, T. S., S. D. Hening, and D. W. Watt (1991), Crack Formation during Laser Cutting of Silicon, **J. Appl. Phys. 69**(2), 983–989.
11. Modest, M. F. (1998), Transient Elastic and Viscoelastic Thermal Stresses During Laser Drilling of Ceramics, **J. Heat Transfer 120**, 892–898.
12. Modest, M. F. (1996), Three-Dimensional, Transient Model for Laser Machining of Ablating/Decomposing Materials, **Int. J. Heat Mass Transfer 39**(2), 221–234.
13. Roy, S., and M. F. Modest (1993), CW Laser Machining of Hard Ceramics — Part I: Effects of Three-Dimensional Conduction and Variable Properties and Various Laser Parameters, **Int. J. Heat Mass Transfer 36**(14), 3515–3528.
14. Boley, B. A., and J. H. Weiner (1960), Theory of Thermal Stresses, Wiley, New York.
15. Thompson, J. F., Z. U. A. Warsi, and C. W. Mastin (1985), Numerical Grid Generation, Foundations and Applications, North-Holland, New York.